Comparative Evaluation of Different Cables for Magnetic Couplers in Inductive Power Transfer Systems

Jesús Acero, *Senior, Member, IEEE,* Ignacio Lope, *Member, IEEE,* Claudio Carretero, *Senior, Member, IEEE,* Héctor Sarnago, *Senior, Member, IEEE,* and José Miguel Burdío, *Senior, Member, IEEE*

***Abstract*—Copper litz wires are widely used in wireless charging stations of light-duty electric vehicles. This type of cable is specifically mentioned in the SAE J2954 standard. However, details as the number and diameter of strands, or the material of conductors are not mentioned in the standard, which makes room to address some research and innovations. In this work, several alternatives to the traditional copper-litz wires are analyzed. Specifically, aluminum litz wire, copper-clad aluminum litz wire, and copper tubes are considered as alternatives to standard litz wire for the mentioned application. Potential benefits of the considered alternatives could include weight and cost savings. However, these advantages could not be enough to justify a wiring change if the resistance of the power pads increases and, equivalently, the efficiency of the electromagnetic power transfer decreases. For this reason, a model of the parasitic resistance of windings is proposed by combining the analytical ac resistance of two-layered round strands and finite element simulations. This model is used to obtain a figure of merit related with the efficiency of the electromagnetic energy transfer which is used to compare the different cables. Apart from efficiency, thermal behavior, cost and weight are also considered for comparison purposes. As a result, some conclusions about the suitability of each cable with respect to the operating frequency range are extracted.**

***Index Terms*—Ac Resistance, Wireless Power Transfer, Electromagnetic Simulation.**

I. Introduction

CURRENTLY, the energy transition towards a low hydrocarbon-dependency scenario is being leaded by electrical mobility in response to the environmental impact of the gas emissions, and taking advantage of the sustainable energy generation by means of renewable sources. Following a decade of rapid growth, the future prospections translate to estimated cumulative sales of electric vehicles (EVs) of more than fifty million by 2025 [1]. Following the evolution of other battery-powered applications, as smartphones, contactless charging by inductive power transfer (IPT) is progressively penetrating in the electrical mobility market due to the advantages of the wireless technology. However, the deployment of EV wireless chargers is associated with several challenges mainly derived from the high voltage, high magnetic field and high power requirements, which translate into cost and safety issues. These challenges have triggered an intense research activity in this field in the last years [2]–[14].

Design and manufacturing of EV chargers should be in compliance with the existing regulatory standards. In the field of smartphones, the adoption of the *Qi* standard boosted the interoperability and the popularization of wireless charging in any scenario of the daily life. Regarding EV wireless chargers, the Society of Automobile Engineers (SAE) launched the SAE J2954 standard [15]. This standard establishes an implementation framework mainly focused on achieving interoperability between stationary charging stations and users. Specifications collected in the SAE J2954 standard include also aspects as the operating frequency, performance, efficiency targets according to power classes, positioning requirements, geometrical and electrical parameters, and power pad arrangement guidelines. Among those, the standard considers aspects as the assembly topology (single-coil or multi-coil, polarized or non-polarized), dimensions, self-inductance values by power classes, number of turns, cabling and ferrite arrangement. Moreover, the SAE J2954 standard sets the litz wire as the cabling structure for windings. However, apart from the cable diameter ϕ_c (being $\phi_c = 5\,\mathrm{mm}$ the diameter value recommended in some cases), the number, diameter and material of strands are not specified in the standard.

Copper litz wire is present in many power electronics applications due to its superior performance at operating frequencies in the range of tens to hundreds of kHz [16]. However, the use of multi-stranded wires implies an extra cost with respect to single-conductor wires due to the added manufacturing cost incurred by the stranding and twisting processes. The relevance of the litz wire is echoed by a remarkable research activity, most of them focused on modelling the losses phenomena in such as intricate structure [17]–[27].

Currently, aluminum and copper-clad aluminum (CCA) litz wires are often part of the product portfolio of wire manufacturers. The interest of these products lies in the cost and weight savings, which potentially can be achieved in some applications. Benefits of aluminum litz wires and other related solutions were firstly analyzed in [28]. Apart from this pioneering analysis, aluminum litz-wire works have

Jesús Acero, Héctor Sarnago and José Miguel Burdío are with the Department of Electronic Engineering and Communications, I3A, Universidad de Zaragoza, Zaragoza, Spain, (e-mail: jacero@unizar.es).

Ignacio Lope and Claudio Carretero are with the Department of Applied Physiscs, I3A, Universidad de Zaragoza, Zaragoza, Spain.

This work was partly supported by the Spanish MICINN under Projects AEI PID2022-136621OB-I00, PID2019-103939RB-I00, PDC2021-120898-I00, TED2021-129274B-I00, CPP2021-008938, ISCIII PI21/00440, co-funded by EU through FEDER and NextGenerationEU/PRTR programs, by the DGA-FSE, and by the BSH Home Appliances Group. Authors would like to acknowledge the use of Servicio General de Apoyo a la Investigación-SAI, Universidad de Zaragoza

Manuscript received xxx xx, xxxx; revised xxx xx, xxxx.

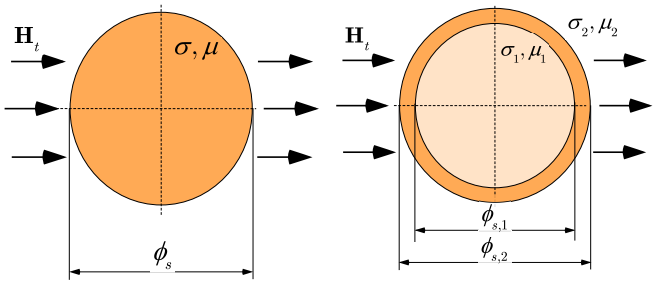

(a) (b)

Fig. 1. Section of a simple and two-layered strands in a transversal uniform magnetic field. (a) Simple strand. (b) Two-layered conductor.

rarely been contributed to the literature, and exceptions are circumscribed to some conference communications [29]–[33]. A similar situation is observed with CCA litz wires [34] whose use for EVs chargers has been recently reported [35].

Copper tubes have also been used in high power applications at several hundreds of kHz or even at some MHz, especially in the field of the induction heating [36], [37]. However, the use of copper tubes as an alternative to copper litz wires for IPT applications has barely been considered in the literature, and the existing works are rather preliminary approaches [38] or solutions focused on improving the quality factor Q in some specific applications [39], [40]. The idea of copper tubes has been also extended to litz wires [41].

Summarizing, on the one hand some aspects of the cables used in EVs wireless battery chargers are not completely specified in the current standard, leaving margin for selecting and optimizing the cable material or the litz wire structure, including the number and diameter of strands. On the other hand, according to the current literature, aluminum litz wires, CCA litz wires and copper tubes are hardly used for IPT applications and, consequently, frequency-dependent losses for these cables have not been deeply analyzed in the literature. Consequently, this paper aims to analyze the mentioned alternatives for copper litz-wire IPT systems in the frame of the SAE J2954 standard, and it also aims to contribute to the existing state-of-the-art in this field. The analysis mainly focuses on Joule's wire ac losses because they affect the IPT's quality factor and efficiency. Subsidiarily, the paper also analyzes aspects as material, manufacturing costs, or availability.

The paper is organized as follows. The loss model of the considered cables and the winding simulation model are presented in Section II and Section III, respectively. Section IV presents the main experimental results including impedance measurements and validation at power transfer conditions. This section also discuses other aspects as price or weight. The main conclusions of this work are summarized in Section V.

II. Skin and Proximity Effects in Two-Layered Round Conductors

The winding equivalent series resistance (ESR) of a magnetic device includes both dc resistance and ac resistance, which encapsulates skin and proximity effects. Skin effect is the tendency of the current to flow to the surface of the conductors when the frequency is increased. The skin effect can be modeled as a frequency-dependent term that appears as a multiplicative factor of the dc resistance. Proximity effect is a pure ac effect consisting of Joule's losses generated by zero-net currents in a conductor, which in general are induced by the alternating magnetic field generated by the neighbouring conductors. Proximity losses typically occur in multiturn windings. Unlike the skin effect, the contribution of proximity losses is additive, in relation to R_{dc}, rather than multiplicative. Considering the infinitely-long isolated cylindrical conductor shown in Fig. 1a, expressions of the dc by skin and proximity resistances per unit of length (ul) are [42]:

TABLE I
Low and high frequency approximations of Φ_{skin} and Φ_{prox}

	Solid	Two-Layered
$\Phi_{\mathrm{skin,LF}}$	1	1
$\Phi_{\mathrm{skin,HF}}$	$\frac{1}{2}\frac{r_s}{\delta}$	$\frac{1}{2}\left[1+\frac{r_{s,1}^2}{r_{s,2}^2}\left(\frac{\sigma_1}{\sigma_2}-1\right)\right]\left(\frac{r_{s,2}}{\delta_2}\right)$
$\Phi_{\mathrm{prox,LF}}$	$\frac{1}{4}\left(\frac{r_s}{\delta}\right)^4$	$\frac{1}{4}\left[\frac{\sigma_2}{\sigma_1}\left(\frac{r_{s,1}}{\delta_1}\right)^4+\left(\frac{r_{s,2}^4-r_{s,1}^4}{\delta_2^4}\right)\right]$
$\Phi_{\mathrm{prox,HF}}$	$\frac{r_s}{\delta}$	$\left(\frac{r_{s,2}}{\delta_2}\right)$

$$R_{\mathrm{dc\cdot skin,ul}} = R_{\mathrm{dc,ul}} \cdot \Phi_{\mathrm{skin}}\left(r_s/\delta\right) = \frac{1}{\pi r_s^2 \sigma}\Phi_{\mathrm{skin}}\left(r_s/\delta\right), \quad (1)$$

$$R_{\mathrm{prox,ul}} = \frac{4\pi}{\sigma}\Phi_{\mathrm{prox}}\left(r_s/\delta\right)\bar{H}_t^2, \quad (2)$$

where r_s is the radius of the cylindrical conductor, σ is the conductor's electrical conductivity, δ is the skin depth of the fields in the conductor defined as $\delta = \sqrt{2/(\omega\sigma\mu)}$, with μ being the magnetic permeability of the conductor, and ω the angular frequency. Moreover, $\bar{H}_t^2$ is the squared value of the magnetic field per unit of current. Functions Φ_{skin} and Φ_{prox} capture the frequency dependency of skin and proximity resistances and they solely depend on the ratio between the conductor radius and the skin depth (r_s/δ). Both exact and approximate expressions can be found in several references [16], [42], where asymptotic approximations at low frequency (LF, for $r_s/\delta \ll 1$) and high frequency (HF, for $r_s/\delta \gg 1$) regimes for cylindrical conductors, which are of practical interest, can be also found. These approximations are collected in Table I.

Several winding loss models of magnetic devices with solid round wires or litz wires have been proposed on the basis of the LF and HF approximations for solid conductors shown in Table I [43]. In contrast to solid strands, CCA strands and copper tubes are inhomogeneous in the radial direction, which affect to the skin and proximity effects. Fig. 1b shows the cross section of an infinitely-long cylindrical two-layered conductor whose diameters are $\phi_{s,1} = 2\cdot r_{s,1}$ and $\phi_{s,2} = 2\cdot r_{s,2}$, respectively. The electrical conductivity and magnetic permeability of each material are σ_1, μ_1 and σ_2, μ_2, respectively. The corresponding skin depths associated to these properties are δ_1 and δ_2.

As in the case of solid conductors, it is also assumed that the dc by skin and proximity resistances per unit of length of the two-layered conductor can be expressed as follows:

$$R_{\mathrm{dc\cdot skin,ul}} = R_{\mathrm{dc,ul}} \cdot \Phi_{\mathrm{skin}}\left(r_{s,1}, \delta_1, r_{s,2}, \delta_2\right), \tag{3}$$

$$R_{\mathrm{prox,ul}} = \frac{4\pi}{\sigma_2}\Phi_{\mathrm{prox}}\left(r_{s,1}, \delta_1, r_{s,2}, \delta_2\right) \cdot \bar{H}_t^2. \tag{4}$$

In this case the dc resistance is:

$$R_{\mathrm{dc,ul}} = \frac{1}{\pi\left[\sigma_1 r_{s,1}^2 + \sigma_2\left(r_{s,2}^2 - r_{s,1}^2\right)\right]}. \tag{5}$$

Several expressions of $R_{\mathrm{dc\cdot skin,ul}}$ for tubular conductors [44] and bimetallic conductors [45] were proposed in the past. In some cases these references provides polynomial approximations or primitive mathematical functions, which leads to a difficult practical applicability. Alternatively, $R_{\mathrm{dc\cdot skin,ul}}$ can be also derived from the general case of the dc by skin resistance of multilayer round conductors [46]. Considering this approach, an analytical expression of $R_{\mathrm{dc\cdot skin,ul}}$ for the two-layered round conductor was obtained and it is shown in the Appendix A. Despite this formula provides an exact values, mathematical tools are required for obtaining results, and therefore it could have limited applicability in practical engineering. However, as occurs with solid conductors, LF and HF approximations are much easier to use and they could also provide accurate results.

The low frequency regime is equivalent to the dc current conduction. Therefore:

$$\Phi_{\mathrm{skin,LF}} = 1 \qquad r_{s,1}/\delta_1 \ll 1,\ r_{s,2}/\delta_2 \ll 1. \tag{6}$$

Moreover, at sufficient high frequency the current flows almost entirely in the external layer, and at this regime the resistance of the two-layered round conductor is almost identical to that of a solid conductor made of the external material. Therefore [42]:

$$R_{\mathrm{dc\cdot skin,ul,HF}} = R_{\mathrm{dc,ul}} \cdot \Phi_{\mathrm{skin,HF}} \cong \frac{1}{2\pi r_{s,2}\sigma_2\delta_2} \tag{7}$$

and therefore:

$$\Phi_{\mathrm{skin,HF}} = \frac{1}{2}\left[1 + \frac{r_{s,1}^2}{r_{s,2}^2}\left(\frac{\sigma_1}{\sigma_2} - 1\right)\right]\left(\frac{r_{s,2}}{\delta_2}\right) \qquad r_{s,1}/\delta_1 \gg 1, \quad r_{s,2}/\delta_2 \gg 1. \tag{8}$$

Considering (8), it can be deduced that skin losses could be lessened by using two-layered conductors with $\sigma_2 > \sigma_1$, as copper tubes. However, the dc resistance of tubes can be higher than solid wires of identical radius.

Regarding the proximity resistance per unit of length of the two-layered round conductor, as it was aforementioned, an expression similar to (2) is adopted:

$$R_{\mathrm{prox,ul}} = \frac{4\pi}{\sigma_2}\Phi_{\mathrm{prox}}\bar{H}_t^2, \tag{9}$$

where the exact formula of Φ_{prox}, can also be obtained from the multilayer general case [46]. This formula is in the Appendix B. However, as occurred in the previous case, LF and HF approximations are easier to handle in practical engineering. At the LF regime the two-layered round conductor is fully penetrated by the magnetic field and therefore losses are induced in both internal and external layers. Consequently, losses can be obtained on the basis on the proximity resistance of cylindrical solid conductors at LF regime:

$$R_{\mathrm{prox,ul,LF}} = \left[\frac{\pi}{\sigma_1}\left(\frac{r_{s,1}}{\delta_1}\right)^4 + \frac{\pi}{\sigma_2}\left(\frac{r_{s,2}^4 - r_{s,1}^4}{\delta_2^4}\right)\right]\bar{H}_t^2 \qquad r_{s,1}/\delta_1 \ll 1,\ r_{s,2}/\delta_2 \ll 1 \tag{10}$$

This value is used to obtain the expression of $R_{\mathrm{prox,ul,LF}}$, which is also collected in Table I.

Moreover, as in the case of the skin effect, at high frequencies the current is induced only in the outermost layer. Therefore, the HF approximation for two-layered round conductors can be obtained considering the HF approximation in cylindrical solid conductors [42]. The expression of $\Phi_{\mathrm{prox,HF}}$ is also collected in Table I.

Exact expressions of Φ_{skin} and Φ_{prox} for two-layered round conductors are compared with approximations in Fig. 2a and Fig. 2b, respectively. These results corresponds to a 15% CCA conductor with the equivalent cross sectional area of a copper strand of diameter $\phi_s = 0.5$ mm. In these figures the horizontal axis is equal to the radius of the external layer divided by its corresponding skin depth, i.e. $(r_{s,2}/\delta_2)$. Consequently, increasing values of the horizontal axis corresponds to higher frequencies. This representation is adopted because $(r_{s,2}/\delta_2)$ is a factor of $\Phi_{\mathrm{skin,HF}}$ and $\Phi_{\mathrm{prox,HF}}$ for two-layered conductors in Table I. According to Fig. 2a and Fig. 2b, LF and HF approximations are accurate excepting when the strand radius is few times higher than the skin depth. In this case, the error observed in the approximation of Φ_{skin} is the 31%, whereas in the case of solid uniform strands the error is lesser than the 15% [42].

Considering round homogeneous strands this kind of representation makes patent that the functions $\Phi_{\mathrm{skin}}\left(r_s/\delta\right)$ and $\Phi_{\mathrm{prox}}\left(r_s/\delta\right)$ are identical for all diameters and materials. However, in two-layered conductors the invariance of Φ_{skin} and Φ_{prox} only holds in the case of homomorphic strands, for example CCA conductors with equal copper clad percentage, regardless the total diameter.

The influence of copper cladding percentage on the skin and proximity factors is also studied and the results are shown in Fig. 3 for equal dc resistance. The copper percentage ranges from 5% to 50% as they correspond to the available high-tension CCA litz wires of some manufacturers [47]. As it is shown, the influence of frequency is higher than the influence of the copper percentage. In other words, Φ_{skin} and Φ_{prox} are almost invariant with respect to the copper percentage for a selected $(r_{s,2}/\delta_2)$ value. In conclusion, the percentage of copper to aluminum hardly affects the ac resistance for a given dc resistance or, in other words, resistance optimization can be hardly achieved by changing the copper-clad ratio. This

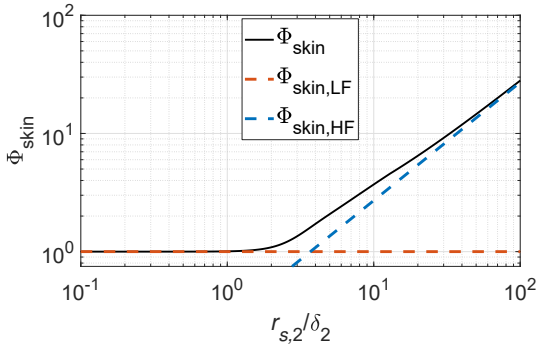

(a)

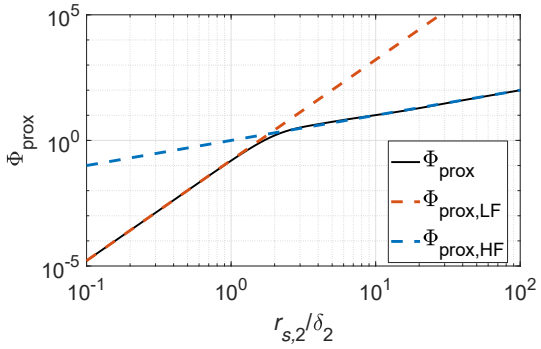

(b)

Fig. 2. Comparison of the exact formula of the skin and proximity factors and their low and high frequency approximations for 15% CCA conductors. (a) Skin factor. (b) Proximity factor.

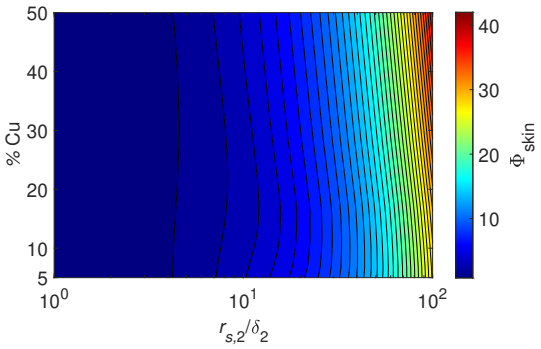

(a)

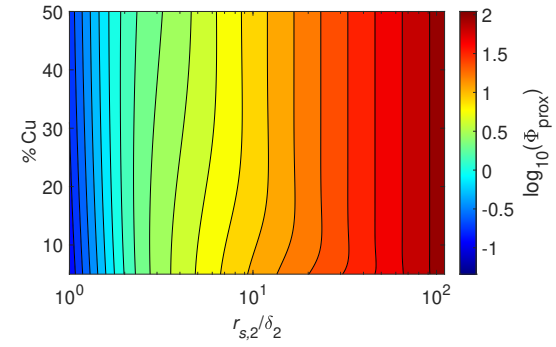

(b)

Fig. 3. Effect of the copper cladding percentage and frequency on the skin and proximity factors. (a) Skin factor. (b) Proximity factor.

result is the basis for the later experimental verification. As it is shown in Fig. 2b and Fig. 3, this result is also valid at the low frequency regime.

III. Winding Loss Model

A loss model of windings with the above considered cables is derived in this section. The objective is to obtain a model valid for litz wires made of copper, aluminum or CCA strands, as well as for copper tubes. IPT systems can include several coupled power pads. Fig. 4 shows the typical arrangement of a magnetic coupler for IPT applications. This arrangement includes the ferrite and the shielding being the considered dimensions compatible with the SAE J2594 standard.

Unlike solenoidal arrangements, the magnetic field generated by this system has a strong 2D dependency. Magnetic field is required not only for calculating the coupling coefficient but also for estimating the proximity losses. A mixed-model strategy that combines Finite Element (FEA) simulations and the resistances of the two-layered round conductors previously presented is used to develop the model. As occurs in other magnetic components, the size of the device is much greater than the size of the involved conductors or strands. For this reason, in order to simulate the system shown in Fig. 4 with a reasonable computational cost the following assumptions are adopted:

- The magnetic field is not modified by the induced currents in the windings. Equivalently, the magnetic field generated by the real winding is identical to the magnetic field generated by an hypothetical ideal lossless winding of the same number of turns, size and geometry.
- The spiral effect of the winding is neglected. Consequently, individual concentric turns are considered.
- The transposition of the strands in the litz wires is perfect and, consequently, all strands are equivalent.
- Ferrites are a perfect lossless magnetic conductor.
- At the interest frequency range, the shielding can be modelled by an Impedance Boundary Condition (IBC).
- In the case of multi winding arrangements, cross-impedance terms are neglected, excepting the mutual inductance. Moreover, all windings are identical.
- At the interest frequency range, centered at $85\,\mathrm{kHz}$, parasitic capacitances are disregarded.

According to these assumptions, in the simulation tool the real conductors are replaced by ideal lossless constant current densities of amplitude $J_w = I_{\mathrm{coil}}/S_c$, where S_c is the cross sectional area of the cable. Moreover, each winding can be considered as the series connection of n_t turns and the parallel connection of n_s equivalent strands. Considering two-layered round conductors, the dc by skin resistance of the i^{th} winding is [43]:

$$R_{\mathrm{dc\cdot skin},i} = \frac{n_t}{n_s} \cdot \mathrm{MLT} \cdot R_{\mathrm{dc,ul}} \cdot \Phi_{\mathrm{skin}}. \tag{11}$$

where MLT is the mean length of the winding's turn.

The proximity resistance of the i^{th} coil is:

$$R_{\mathrm{prox},i} = n_s \cdot \frac{4\pi}{\sigma} \Phi_{\mathrm{prox}} \cdot \left\langle \bar{H}_i^2 \right\rangle, \tag{12}$$

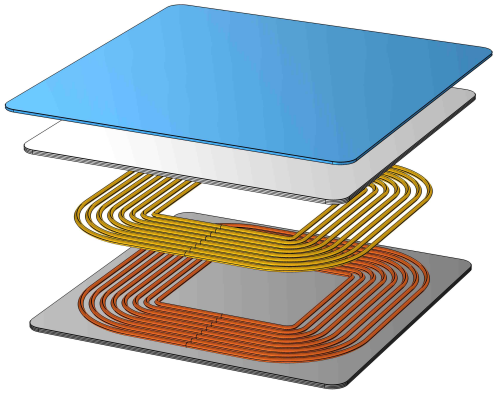

Fig. 4. Image of the 3D finite-element simulation model of the two power pad system for the copper tube case.

where $\langle \bar{H}_i^2 \rangle$ is the average of the squared magnetic field normalized per unit of current in the i^{th} winding. An average is used for capturing the fact that the field is different at each turn. This value is obtained by means of the FEA tool as follows:

$$\langle \bar{H}_i^2 \rangle = \frac{1}{S_c} \int_{V_w} \bar{H}_i^2 \cdot dv_w, \tag{13}$$

where $\bar{H}_i^2$ is the squared modulus of the magnetic field per Ampère in the i^{th} winding, and S_c is the cross-sectional area of the cable. This field can be different in each coil depending on the ferrite arrangement or the presence of the shielding. This value also accounts for total winding length.

Moreover, some power can be dissipated in the shielding, which is translated as an increase of the resistance of the inducing winding, $R_{\mathrm{sh},i}$. This resistance is obtained by means of the FEA tool as follows:

$$R_{\mathrm{sh},i} = \frac{1}{2}\mathrm{Re}\left[\int_{S_{\mathrm{sh}}} \left[\left(\overline{\mathbf{E}}_i \times \overline{\mathbf{H}}_i{}^*\right)\right] \cdot d\vec{\mathbf{S}}_{\mathrm{sh}}\right], \tag{14}$$

where bars over the electrical and magnetic fields indicate per Ampère values.

The total ESR resistance of the i^{th} winding, which should be compared with measurements, is:

$$R_i = R_{\mathrm{dc\cdot skin},i} + R_{\mathrm{prox},i} + R_{\mathrm{sh},i} \tag{15}$$

Apart from these resistances, the simulated values of the self and mutual inductances L_i, M_{ij} will be also obtained. These values are required for obtaining other magnitudes as the coupling coefficient k or the system quality factor Q:

$$Q = \sqrt{Q_1 \cdot Q_2}, \tag{16}$$

where ω is the angular frequency. These magnitudes are used to calculate the factor kQ:

$$kQ = \frac{\omega M_{12}}{\sqrt{R_1 R_2}}. \tag{17}$$

TABLE II
PARAMETERS OF THE CABLES

	n_s	ϕ_s	$\phi_{s,1}$ [µm]	$\phi_{s,2}$	σ	σ_1 [MS/m]	σ_2
Cu litz wire	200	200	–	–	58	–	–
Al litz wire	414	200	–	–	30	–	–
CCA litz wire	304	–	208	220	–	30	58
Copper tube	1	–	4500	6500	–	0	44

which is often considered as a figure of merit for comparing between different power pads [48].

IV. Experimental verification

In order to verify the accuracy of the loss model and to test the performance of the considered cables, several magnetic couplers were designed and tested. The arrangement of the magnetic couplers was in accordance with the SAE J2954 standard vehicle assembly for the power class WPT3 whose coil dimension is $380 \times 380\,\mathrm{mm}$. The experimental setup also comprised a ferrite plane (made of 3C90 ferrite tiles) and aluminum shielding. The electrical conductivity and relative magnetic permeability of the ferrite and the shielding used in simulation were $\sigma_f = 0\,\mathrm{S/m}$, $\mu_{r,f} = 1000$, $\sigma_{\mathrm{Al}} = 30\,\mathrm{MS/m}$, and $\mu_{r,\mathrm{Al}} = 1$, respectively.

The cable considered as reference was a commercial copper litz wire with $n_s = 200$ strands of diameter $\phi_s = 200\,\mu\mathrm{m}$. The dc resistance per metre of this cable is $2.7\,\mathrm{m\Omega/m}$. Due to the manufacturing process, the strands are tightly twisted in a single twisting operation, resulting in a compact tape-shaped cable. Fig. 5a shows a detail of the magnetic coupler prototype with this cable. Other prototypes were designed with the considered alternatives under the premise of similar dc resistance, excepting the copper tube whose dc resistance per metre is $1.3\,\mathrm{m\Omega/m}$ due to the available gauges. Copper tubes correspond to annealed non-electrolytic copper pipes for transporting gas and water in the household ambit, and whose electrical conductivity is lesser than the cabling copper. The parameters of the different cables are shown in Table II. As this table shows, the strand diameters of the different cables are similar and range from $\phi_s = 200\,\mu\mathrm{m}$ (Cu litz wire) to $\phi_s = 220\,\mu\mathrm{m}$ (CCA litz wire). Such diameters were chosen in view of (1) and (2), because dissimilar strands could have very different $R_{\mathrm{dc\cdot skin,ul}}$ and $R_{\mathrm{prox,ul}}$ at a specific frequency. On the other hand, the insulation type of strands was selected according to the working temperature range. In this case the selected insulation was polyurethane, which corresponds to a temperature class of $105\,^{\circ}\mathrm{C}$. Aluminum and CCA litz wires were hand-built in several twisting steps. For this reason, the diameter of these cables is higher than the commercial copper litz wire. The aspect of the different prototypes, including the copper tube prototype, is shown in Fig. 5. In addition, a specific frame was designed to allow both horizontal and vertical displacements of the power pads.

A. Impedance measurements

The purpose of impedance measurements is mainly to test the accuracy of the developed models. Accordingly, the series resistance and inductance are measured by means of the

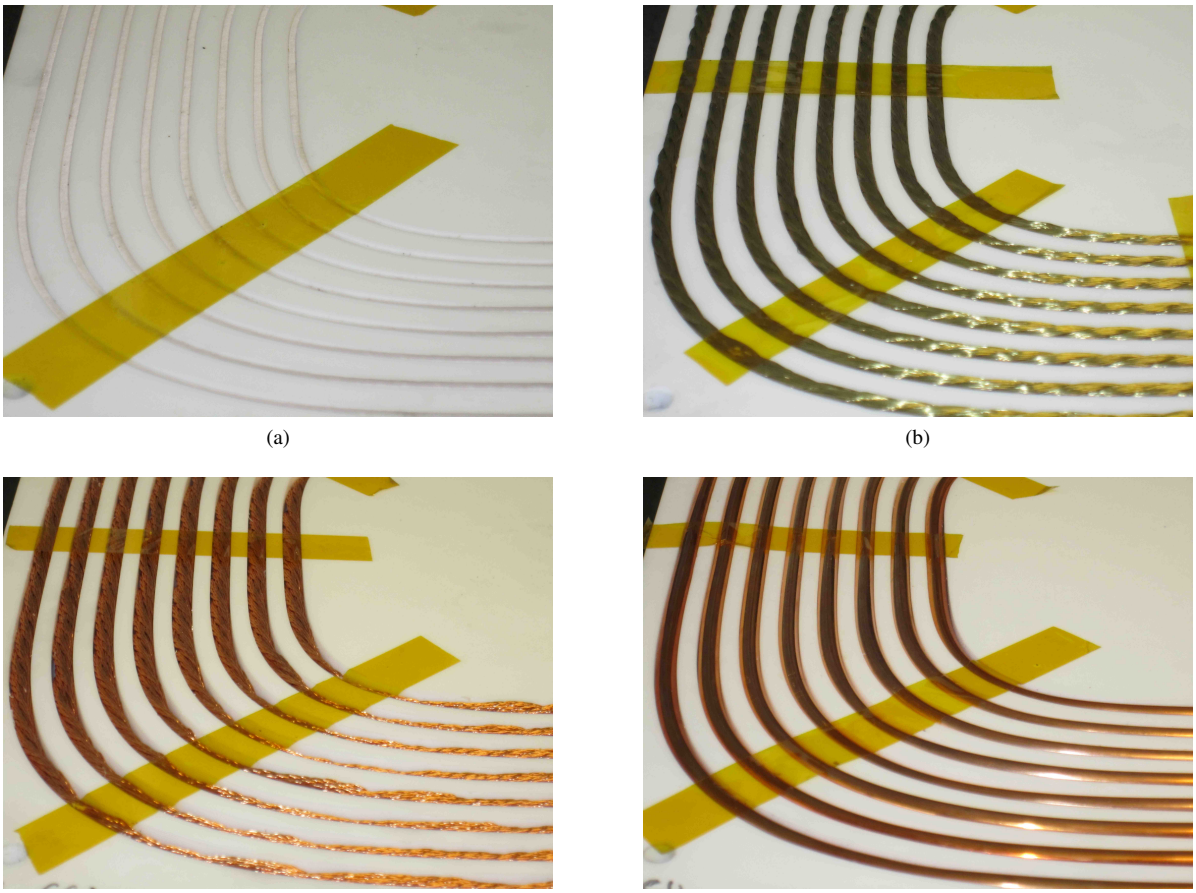

(a) (b) (c) (d)

Fig. 5. Images of the prototypes with the different cables. (a) Copper litz wire. (b) Aluminum litz wire. (c) CCA litz wire. (d) Copper tube.

Keysight E4980A high precision LCR meter. The frequency of measurements ranged from $10\,\mathrm{kHz}$ to $500\,\mathrm{kHz}$. Calculated and measured resistances for the different prototypes are shown in Fig. 6a, and the ac resistance, R/R_{dc}, is shown in Fig. 6b. The resistance of the two-layered conductors is calculated with the exact expression. Results show that, in general, the model predictions are quite accurate, especially in the case of the copper tube. However, regarding the litz wire, the model is more accurate in the case of cables with several twisting steps, whose strands are more equivalent than in the single twisting case.

Litz wires present lower resistance at the intermediate frequency range. However, no particular litz wire is clearly better than others. According to the Fig. 6a, aluminum and CCA litz wires could improve the performance of the copper litz wires. However, the ac resistance also evidences that the three considered litz wires are quite similar. This result also reflects the fact that the CCA litz wire is under a lower magnetic field than the other litz wires, as corresponds to its highest cross-sectional area (13), and therefore lower proximity losses (9). The values of $\langle \bar{H}_i^2 \rangle$, S_c and MLT for each cable obtained by simulation are shown in Table III. In this table, the magnitude referred to the magnetic field corresponds to the average defined in (13).

The copper tube resistance is lower at frequencies higher

TABLE III
SIMULATED FIELD AND GEOMETRIC VALUES OF COILS

	Cu litz	Al litz	CCA litz	Copper tube
MLT [m]	1.01	1.01	1.01	1.01
$\langle \bar{H}_i^2 \rangle$ $[\mathrm{k \cdot m^{-1}}]$	43	37.4	27.3	26.2
S_c $[\mathrm{mm^2}]$	15	23.7	33.2	33.2

that $350\,\mathrm{kHz}$. Despite copper tubes being penalized at the intermediate frequency range due to the high skin effect, the single-strand intrinsic characteristic of the copper tube favours a moderate proximity resistance at the highest frequency range.

The inductance measurements (Fig. 6c) show that the cable diameter also has a small influence on the self inductance in such a way that the smaller the diameter is, the higher the inductance.

Considering two power pads, measurements of k and Q factors were also carried out for several vertical distances d and lateral misalignments l. The calculation of the mentioned factors requires the mutual inductance between coils, which is experimentally obtained by operating with the inductances measured according to the in-phase and anti-phase connections of coils:

$$M = \frac{L_{\mathrm{i\_p}} - L_{\mathrm{a\_p}}}{4} \tag{18}$$

This article has been accepted for publication in IEEE Transactions on Industry Applications. This is the author's version which has not been fully edited and content may change prior to final publication. Citation information: DOI 10.1109/TIA.2023.3344686

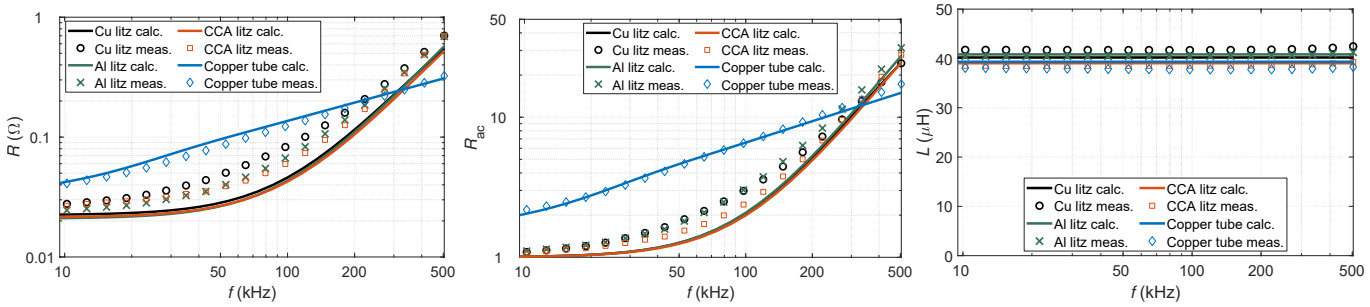

Fig. 6. Measured and calculated resistances of the prototypes with the considered cables. (a) Resistance. (b) Ac resistance. (c) Inductance.

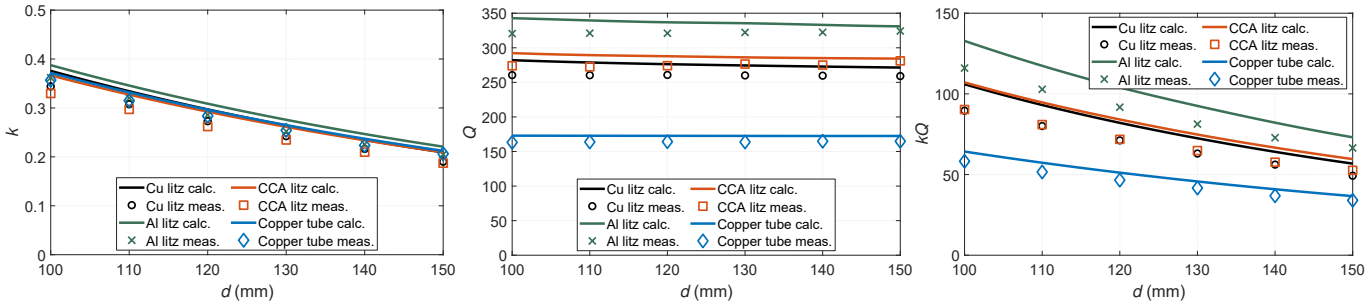

Fig. 7. Comparison of simulated and measured results for concentrically placed power pads at different vertical distances at 85 kHz. (a) k. (b) Q. (c) kQ.

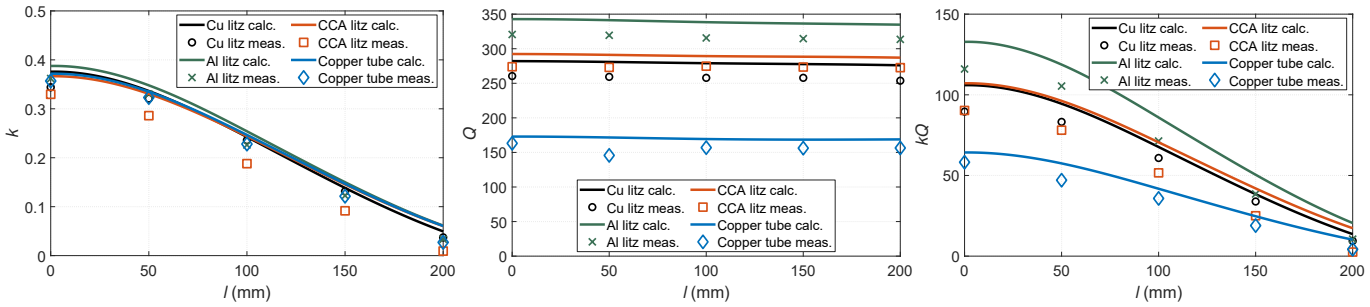

Fig. 8. Comparison of simulated and measured results for power pads at different misalignments at 85 kHz. (a) k. (b) Q. (c) kQ.

In the first case, the two power pads are horizontally aligned and the vertical distance is increased from $d = 100\,\mathrm{mm}$ to $150\,\mathrm{mm}$ with the frame shown in Fig. 9. Inductances were measured at $85\,\mathrm{kHz}$. Simulated and measured results are shown in Fig. 7. Moreover, in the second case the power pads are placed at a vertical distance $d = 100\,\mathrm{mm}$ and the horizontal misalignment is varied from $l = 0\,\mathrm{mm}$ to $200\,\mathrm{mm}$. Simulated and measured results are shown in Fig. 8. In both scenarios the coupling factor decreases as the distance between coils increases, whereas the quality factor is almost constant. The simulated quality factor is higher than the measured as corresponds to the lower simulated resistance. As it is shown, the kQ factor of the aluminum litz wire is higher than the others at the considered frequency. Simulated and measured values follow the same tendencies.

B. *Validation at power transfer conditions*

The performance of the considered cables was tested at power transfer conditions. The prototype consisted of a full bridge inverter with IXYS IXFN 48N50 MOSFETS, a series/series compensation network, a Microsemi MSCDC100H120AG SiC Diode Full Bridge Power Module, and a resistor load of value $R_{load} = 8.8\,\Omega$. The power is therefore controlled by means of the dc feeding voltage, which in this case is supplied by a commercial power supply. The switching frequency, $f_s = 85\,\mathrm{kHz}$, is set at the resonant condition for the cable with the lowest inductance, in this case the copper tube. Consequently at this frequency the power pads with the other cables at $f_s = 85\,\mathrm{kHz}$ are in ZVS condition. The resultant capacitor is $C_p = C_s = 85.2\,\mathrm{nF}$

An image of the experimental setup and an oscilloscope screenshot are shown in Fig. 9 and Fig. 10, respectively. This figure represents the main waveforms at $f_s = 85.0\,\mathrm{kHz}$ for

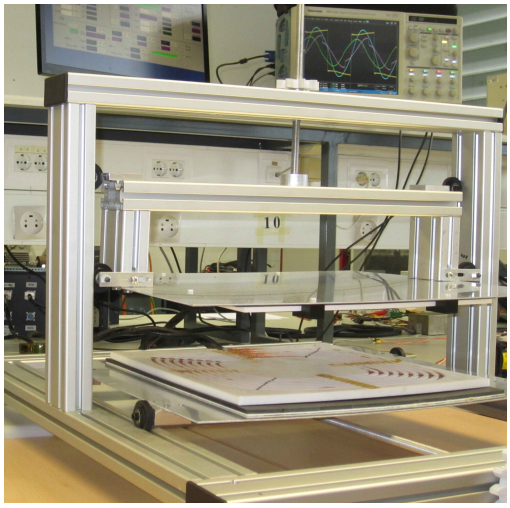

Fig. 9. Image of the experimental setup including the magnetic coupler and oscilloscope.

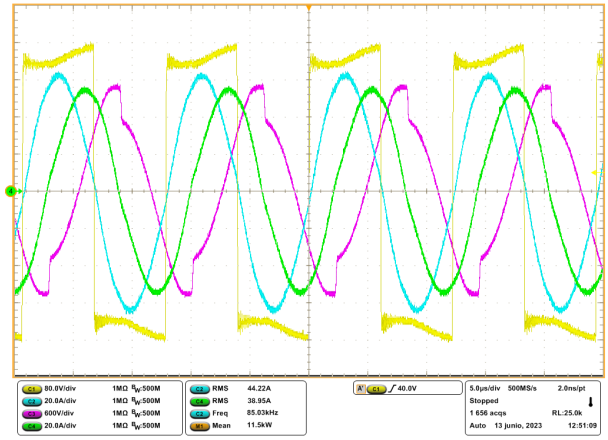

Fig. 10. Main experimental waveforms at $P_o = 11.5\,\mathrm{kW}$.

an output power of $P_o = 11.5\,\mathrm{kW}$, which corresponds to an input voltage of $V_{in} = 300\,\mathrm{V}$, a primary current of $I_{p,\mathrm{rms}} = 44.22\,\mathrm{A}$, the voltage at terminals of the secondary power pad (whose peak value is higher than $1500\,\mathrm{V}$), and a secondary current of $I_{s,\mathrm{rms}} = 38.95\,\mathrm{A}$.

At these conditions the measured efficiency of the inductive electromagnetic power transfer, $\eta_{\mathrm{em,meas}}$, for the different cables is shown in Table IV. The efficiency was estimated by means of the captured voltage and current waveforms at the terminals of the power pads. Moreover, the whole system (including the inverter, the magnetic coupler with compensation capacitors, and the load) was also simulated by means of LTSpice, where the impedance values of the power pads were extracted by the finite element simulations. The simulated electromagnetic efficiency $\eta_{\mathrm{em,sim}}$ is also obtained with the voltage and current simulated waveforms at the terminals of the power pads, and are also shown in Table IV.

The steady-state temperature of the prototypes transferring $P_o = 5\,\mathrm{kW}$ was taken with a thermographic camera and the results are shown in Fig. 11. As expected, the highest temperature corresponds to the inner turns of power pads

TABLE IV
COMPARISON OF PARAMETERS

	Cu litz	Al litz	CCA litz	Copper tube
$\eta_{\mathrm{em,meas}}(\%)$	95.2	95.8	95.0	88.8
$\eta_{\mathrm{em,sim}}(\%)$	96.1	96.6	96.0	89.1
$\eta_{\mathrm{system,meas}}(\%)$	89.3	89.7	89.6	83.0
$T(^\circ\mathrm{C})$	39.6	36.5	36.8	49.2
weight[1] (g)	458.5	286.0	316.6	630.4
relative cost[1] (%)	100	40	45	18

[1] Normalized at the same R_{dc}.

because they are under the highest magnetic field and, consequently, the highest proximity losses. In any case, copper tubes present the highest temperature among the tested prototypes, as corresponds with its lowest efficiency. Moreover, the observed copper litz temperature is higher than the other litz wires. Apart from efficiency, this result points that the steady-state temperature also depends on the manufacturing process of the cable, and tightly cables could have more difficulties to evacuate the dissipated power.

C. Discussion

Two aspects are discussed in this section: the accuracy of the modeling and the suitability of each cable for practical application regarding aspects such as performance, weight, and cost.

As it was above presented, a loss model was developed considering the ac losses in round strands and assuming equivalence of strands in the case of multi-strand arrangements. The results presented in Fig. 6a and Fig. 6b show that the loss model is less accurate in the case of litz wires tightly twisted in one step, whereas accuracy increases for the hand-made cables twisted in several steps. These results agree with other existing works about litz wires. Moreover, a remarkable accuracy is observed in the case of the copper tube, which corresponds to a single strand case.

Table IV shows a comparison between several parameters of the considered cables. The measured electromagnetic efficiency, $\eta_{\mathrm{em,meas}}$, of the different litz wires are very similar as corresponds to the simulated results, and the efficiency with copper tube is considerably lower than the others. This table also shows the efficiency of the complete system calculated by dividing the power dissipated in the resistance by the power supplied by the dc power supply. As it is shown, for the litz wires the losses in the magnetic couplers are similar to the losses in the other elements of the system, and these losses in the electronics are similar in all cases.

Regarding temperature, the steady-state temperature not only depends on the efficiency but also on the thermal conditions of the power pad. Moreover, the operating temperature of litz wires is restricted by the maximum enameling temperature, for example, $155\,^\circ\mathrm{C}$. However, such limitation doesn't apply to copper tubes because they are commercially unenamelled available. In relation to weight, considering that the density of aluminum is one third of the copper density, weight savings of about a third percent could theoretically be achieved in windings by replacing copper with aluminum wires. The Table

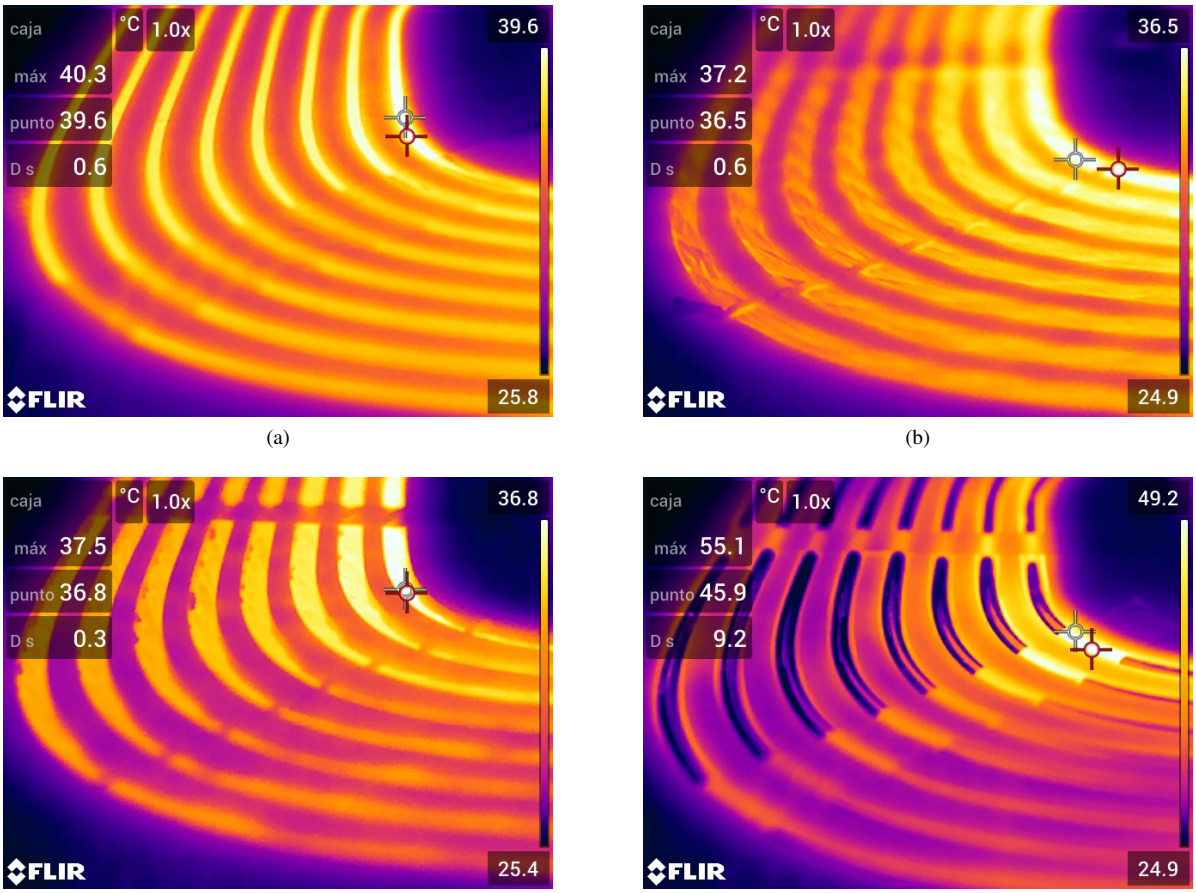

Fig. 11. Thermographic images of the prototypes. (a) Copper litz wire. (b) Aluminum litz wire. (c) CCA litz wire. (d) Copper tube.

IV also collects the calculated weight of each winding considering the volume of the involved metals and their densities normalized at the same dc resistance. The aluminum winding is the lightest, however aluminum winding also has the highest number of strands, and therefore the weight saving is lesser than the one-third expected. It is also worth to mention the high weight of the copper-tube winding.

The cost of each cable mainly depends on the price of the Cu and Al commodity prices and also on the manufacturing process. The manufacturing process of the three considered litz wires is very similar because it encapsulates similar steps, such as wire drawing, enameling, and stranding. Moreover, reliable connections to Al wires are widely used for years and they don't incur extra costs compared with copper litz wires. Currently, the cost of an aluminum-litz wire winding could be lesser than the 40% of the equivalent copper litz-wire winding, and the cost of an aluminum-copper-clad-litz wire winding could be the lesser than the 45% of the equivalent copper litz-wire winding. The copper tube is worthy of special mention as it had the lowest final product price, which can be less than the 20% of the equivalent copper litz wire, mainly due to its simpler manufacturing process. Prices are also collected in Table IV, where the copper litz has been considered as the reference.

The parameters compared in Table IV are also represented in the radar chart shown in Fig. 12, where, instead of efficiencies, the inefficiencies $1-\eta_{em}, 1-\eta_{system}$, have been considered. Therefore, in this diagram, for a particular cable, the smaller the area is, the more suitable the cable. According to this interpretation, aluminum-copper-clad and aluminum-litz wires could represent a balanced option.

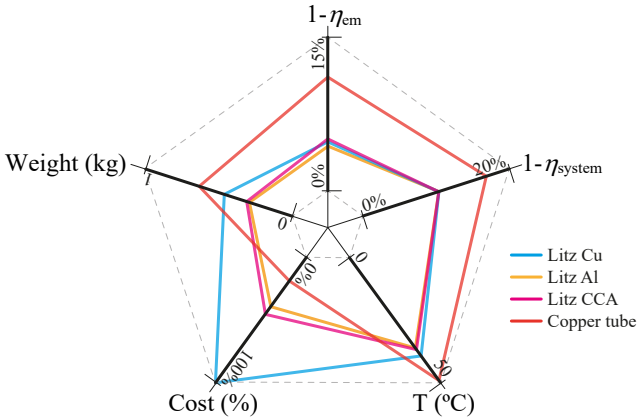

Fig. 12. Radar chart of the different cable alternatives.

V. Conclusion

In this work the series resistance of several cables for IPT magnetic couplers are modeled and compared. The considered alternatives were three litz wire cables (manufactured with copper, aluminum and copper clad aluminum strands) and copper tube, all of them with similar dc resistance. A loss model based on the combination of analytical results, including two-layered conductors, and FEA simulations was also derived to predict the resistances. Both theoretical and experimental results evidence that the resistance of the litz wires was quite similar at the considered frequency range. Consequently, the quality and coupling factors of the considered litz wires are also similar, which determines similar efficiencies. Therefore, other factors, as price, weight, steady-state temperature, or maximum temperature, could be relevant for a specific application. Considering these factors, aluminum litz wire could be a balanced choice between efficiency, cost and weight. Copper tubes have an unbeatable price and maximum temperature but their efficiency is the lowest at the considered frequency regime. Copper tubes also open the possibility of cooling by water. However, copper tubes could represent an interesting alternative at frequencies of several hundreds of kHz, which could be of interest in the near future in view of the power capability and switching frequency tendencies of power electronics.

Appendix A
Exact expression of the dc by skin resistance of a two-layered round conductor

Considering the geometry shown in Fig. 1b, the exact expression of $R_{\mathrm{dc\cdot skin,ul}}$ is:

$$R_{\mathrm{dc\cdot skin,ul}} = \mathrm{Re}\left\{2\pi\left[r_{s,1}\cdot\frac{\sigma_1}{k_1}\cdot\frac{J_1\left(k_1\cdot r_{s,1}\right)}{J_0\left(k_1\cdot r_{s,1}\right)}\cdot\frac{P_1}{P_2} + \frac{\sigma_2}{k_2}\cdot\frac{P_3\cdot P_4 - P_5}{P_2}\right]\right\}^{-1} \tag{19}$$

where

$$k_i = \sqrt{-j\omega\sigma_i\mu_i} \quad i = 1,2 \tag{20}$$

$$\begin{aligned}
P_1 &= P_3\cdot J_1\left(k_2\cdot r_{s,1}\right) - Y_0\left(k_2\cdot r_{s,1}\right)\\
P_2 &= P_3\cdot J_0\left(k_2\cdot r_{s,2}\right) - Y_0\left(k_2\cdot r_{s,2}\right)\\
P_3 &= \frac{P_6 - P_7}{P_8 - P_9}\\
P_4 &= r_{s,2}\cdot J_1\left(k_2\cdot r_{s,2}\right) - r_{s,1}\cdot J_1\left(k_2\cdot r_{s,1}\right)\\
P_5 &= r_{s,2}\cdot Y_1\left(k_2\cdot r_{s,2}\right) - r_{s,1}\cdot Y_1\left(k_2\cdot r_{s,1}\right)\\
P_6 &= \mu_2\cdot k_1\cdot Y_0\left(k_2\cdot r_{s,1}\right)\cdot J_1\left(k_1\cdot r_{s,1}\right)\\
P_7 &= \mu_1\cdot k_2\cdot J_0\left(k_1\cdot r_{s,1}\right)\cdot Y_1\left(k_2\cdot r_{s,1}\right)\\
P_8 &= \mu_2\cdot k_1\cdot J_0\left(k_2\cdot r_{s,1}\right)\cdot J_1\left(k_1\cdot r_{s,1}\right)\\
P_9 &= \mu_1\cdot k_2\cdot J_0\left(k_1\cdot r_{s,1}\right)\cdot J_1\left(k_2\cdot r_{s,1}\right)
\end{aligned} \tag{21}$$

Functions J_ν and Y_ν are Bessel functions of first and second kind and ν^{th} order, respectively.

Appendix B
Exact expression of the proximity resistance of a two-layered round conductor

Proximity losses are induced in the isolated and infinitely-long two-layered round conductor of Fig. 1b when is under a spatially-uniform time-dependent magnetic field of amplitude $\bar{H}_s$ per unit of current. In these conditions, proximity losses can be represented by means of the following resistance:

$$\begin{aligned}
R_{\mathrm{prox,ul}} &= \Phi_{\mathrm{prox}}\cdot\bar{H}_s^2\\
&= 2\pi\cdot\sigma_2\cdot\omega^2\cdot\left(C_1 + C_2 + C_3 + C_4\right)\cdot\bar{H}_s^2
\end{aligned} \tag{22}$$

where

$$\begin{aligned}
C_1 = \frac{C_a\cdot C_a^*}{\sqrt{2}\cdot\xi_2}\times\{&-r_{s,2}\left[ber_1\left(\xi_2\cdot r_{s,2}\right)\cdot ber_2\left(\xi_2\cdot r_{s,2}\right)\right.\\
&+ bei_1\left(\xi_2\cdot r_{s,2}\right)\cdot bei_2\left(\xi_2\cdot r_{s,2}\right)\\
&- ber_1\left(\xi_2\cdot r_{s,2}\right)\cdot bei_2\left(\xi_2\cdot r_{s,2}\right)\\
&\left.+ber_2\left(\xi_2\cdot r_{s,2}\right)\cdot bei_1\left(\xi_2\cdot r_{s,2}\right)\right]\\
&+ r_{s,1}\left[ber_1\left(\xi_2\cdot r_{s,1}\right)\cdot ber_2\left(\xi_2\cdot r_{s,1}\right)\right.\\
&+ bei_1\left(\xi_2\cdot r_{s,1}\right)\cdot bei_2\left(\xi_2\cdot r_{s,1}\right)\\
&- ber_1\left(\xi_2\cdot r_{s,1}\right)\cdot bei_2\left(\xi_2\cdot r_{s,1}\right)\\
&\left.+ber_2\left(\xi_2\cdot r_{s,1}\right)\cdot bei_1\left(\xi_2\cdot r_{s,1}\right)\right]\}
\end{aligned} \tag{23}$$

$$\begin{aligned}
C_2 = \frac{C_b\cdot C_b^*}{\sqrt{2}\cdot\xi_2}&\\
\times\{&-r_{s,2}\left[ker_1\left(\xi_2\cdot r_{s,2}\right)\cdot ker_2\left(\xi_2\cdot r_{s,2}\right)\right.\\
&+ kei_1\left(\xi_2\cdot r_{s,2}\right)\cdot kei_2\left(\xi_2\cdot r_{s,2}\right)\\
&- ker_1\left(\xi_2\cdot r_{s,2}\right)\cdot kei_2\left(\xi_2\cdot r_{s,2}\right)\\
&\left.+ker_2\left(\xi_2\cdot r_{s,2}\right)\cdot kei_1\left(\xi_2\cdot r_{s,2}\right)\right]\\
&+ r_{s,1}\left[ker_1\left(\xi_2\cdot r_{s,1}\right)\cdot ker_2\left(\xi_2\cdot r_{s,1}\right)\right.\\
&+ kei_1\left(\xi_2\cdot r_{s,1}\right)\cdot kei_2\left(\xi_2\cdot r_{s,1}\right)\\
&- ker_1\left(\xi_2\cdot r_{s,1}\right)\cdot kei_2\left(\xi_2\cdot r_{s,1}\right)\\
&\left.+ker_2\left(\xi_2\cdot r_{s,1}\right)\cdot kei_1\left(\xi_2\cdot r_{s,1}\right)\right]\}
\end{aligned} \tag{24}$$

$$\begin{aligned}
C_3 = \frac{\mathrm{Re}\left(C_a\right)\cdot\mathrm{Re}\left(C_b\right) + \mathrm{Im}\left(C_a\right)\cdot\mathrm{Im}\left(C_b\right)}{\sqrt{2}\cdot\xi_2}&\\
\times\{&r_{s,2}\left\{kei_1\left(\xi_2\cdot r_{s,2}\right)\cdot\left[ber_2\left(\xi_2\cdot r_{s,2}\right) + bei_2\left(\xi_2\cdot r_{s,2}\right)\right]\right.\\
&+ ker_1\left(\xi_2\cdot r_{s,2}\right)\cdot\left[ber_2\left(\xi_2\cdot r_{s,2}\right) - bei_2\left(\xi_2\cdot r_{s,2}\right)\right]\\
&- ber_1\left(\xi_2\cdot r_{s,2}\right)\cdot\left[kei_2\left(\xi_2\cdot r_{s,2}\right) - ker_2\left(\xi_2\cdot r_{s,2}\right)\right]\\
&\left.+bei_1\left(\xi_2\cdot r_{s,2}\right)\cdot\left[kei_2\left(\xi_2\cdot r_{s,2}\right) + ker_2\left(\xi_2\cdot r_{s,2}\right)\right]\right\}\\
&- \{r_{s,1}\left\{kei_1\left(\xi_2\cdot r_{s,1}\right)\cdot\left[ber_2\left(\xi_2\cdot r_{s,1}\right) + bei_2\left(\xi_2\cdot r_{s,1}\right)\right]\right.\\
&+ ker_1\left(\xi_2\cdot r_{s,1}\right)\cdot\left[ber_2\left(\xi_2\cdot r_{s,1}\right) - bei_2\left(\xi_2\cdot r_{s,1}\right)\right]\\
&- ber_1\left(\xi_2\cdot r_{s,1}\right)\cdot\left[kei_2\left(\xi_2\cdot r_{s,1}\right) - ker_2\left(\xi_2\cdot r_{s,2}\right)\right]\\
&\left.+bei_1\left(\xi_2\cdot r_{s,1}\right)\cdot\left[kei_2\left(\xi_2\cdot r_{s,1}\right) + ker_2\left(\xi_2\cdot r_{s,1}\right)\right]\right\}\}
\end{aligned} \tag{25}$$

$$
\begin{aligned}
C_4 = & \frac{\mathrm{Re}\left(C_a\right) \cdot \mathrm{Im}\left(C_b\right) - \mathrm{Im}\left(C_a\right) \cdot \mathrm{Re}\left(C_b\right)}{\sqrt{2} \cdot \xi_2} \\
& \times \{r_{s,2} \left\{ker_1\left(\xi_2 \cdot r_{s,2}\right) \cdot \left[ber_2\left(\xi_2 \cdot r_{s,2}\right) + bei_2\left(\xi_2 \cdot r_{s,2}\right)\right]\right. \\
& - kei_1\left(\xi_2 \cdot r_{s,2}\right) \cdot \left[ber_2\left(\xi_2 \cdot r_{s,2}\right) - bei_2\left(\xi_2 \cdot r_{s,2}\right)\right] \\
& - ber_1\left(\xi_2 \cdot r_{s,2}\right) \cdot \left[ker_2\left(\xi_2 \cdot r_{s,2}\right) + kei_2\left(\xi_2 \cdot r_{s,2}\right)\right] \\
& \left. + bei_1\left(\xi_2 \cdot r_{s,2}\right) \cdot \left[ker_2\left(\xi_2 \cdot r_{s,2}\right) - kei_2\left(\xi_2 \cdot r_{s,2}\right)\right]\right\} \\
& - \{r_{s,1} \left\{ker_1\left(\xi_2 \cdot r_{s,1}\right) \cdot \left[ber_2\left(\xi_2 \cdot r_{s,1}\right) + bei_2\left(\xi_2 \cdot r_{s,1}\right)\right]\right. \\
& - ker_1\left(\xi_2 \cdot r_{s,1}\right) \cdot \left[ber_2\left(\xi_2 \cdot r_{s,1}\right) - bei_2\left(\xi_2 \cdot r_{s,1}\right)\right] \\
& - ber_1\left(\xi_2 \cdot r_{s,1}\right) \cdot \left[ker_2\left(\xi_2 \cdot r_{s,1}\right) + kei_2\left(\xi_2 \cdot r_{s,2}\right)\right] \\
& \left. + bei_1\left(\xi_2 \cdot r_{s,1}\right) \cdot \left[ker_2\left(\xi_2 \cdot r_{s,1}\right) - kei_2\left(\xi_2 \cdot r_{s,1}\right)\right]\right\}\}
\end{aligned} \tag{26}
$$

$$
\begin{aligned}
C_a = & 2r_{s,2}/\{[-I_1\left(k_2 \cdot r_{s,2}\right) + k_2 \cdot r_{s,2} \cdot I_0\left(k_2 \cdot r_{s,2}\right) \\
& + P_{10} \cdot K_1\left(k_2 \cdot r_{s,2}\right) + k_2 \cdot r_{s,2} \cdot K_0\left(k_2 \cdot r_{s,2}\right)]/\mu_2 \\
& + [I_1\left(k_2 \cdot r_{s,2}\right) - P_{10} \cdot K_1\left(k_2 \cdot r_{s,2}\right)]/\mu_0\}
\end{aligned} \tag{27}
$$

$$
C_b = -P_{10} \cdot C_a \tag{28}
$$

$$
\begin{aligned}
P_{10} = & \{\mu_2 \cdot I_1\left(k_2 \cdot r_{s,1}\right) \\
& \times [-I_1\left(k_1 \cdot r_{s,1}\right) + k_1 \cdot r_{s,1} \cdot I_0\left(k_1 \cdot r_{s,1}\right)] \\
& - \mu_1 \cdot I_1\left(k_1 \cdot r_{s,1}\right) \\
& \times [-I_1\left(k_2 \cdot r_{s,1}\right) + k_2 \cdot r_{s,1} \cdot I_0\left(k_2 \cdot r_{s,1}\right)]\} \\
& \times 1/\{\mu_2 \cdot K_1\left(k_2 \cdot r_{s,1}\right) \\
& \times [-I_1\left(k_1 \cdot r_{s,1}\right) + k_1 \cdot r_{s,1} \cdot I_0\left(k_1 \cdot r_{s,1}\right)] \\
& + \mu_1 \cdot I_1\left(k_1 \cdot r_{s,1}\right) \\
& \times [K_1\left(k_2 \cdot r_{s,1}\right) + k_2 \cdot r_{s,1} \cdot K_0\left(k_2 \cdot r_{s,1}\right)]\}
\end{aligned} \tag{29}
$$

$$
\begin{aligned}
ber_\nu\left(u\right) &= \mathrm{Re}\left[J_\nu\left(e^{j\frac{3\pi}{4}} \cdot u\right)\right] \\
bei_\nu\left(u\right) &= \mathrm{Im}\left[J_\nu\left(e^{j\frac{3\pi}{4}} \cdot u\right)\right] \\
ker_\nu\left(u\right) &= \mathrm{Re}\left[e^{-j\frac{\pi}{2}\nu} \cdot K_\nu\left(e^{j\frac{\pi}{4}} \cdot u\right)\right] \\
kei_\nu\left(u\right) &= \mathrm{Im}\left[e^{-j\frac{\pi}{2}\nu} \cdot K_\nu\left(e^{j\frac{\pi}{4}} \cdot u\right)\right]
\end{aligned} \tag{30}
$$

$$
\xi_i = \sqrt{\omega\sigma_i\mu_i} \quad i = 1, 2 \tag{31}
$$

Moreover, functions I_ν and K_ν are modified Bessel functions of first and second kind and ν^{th} order, respectively.

REFERENCES

[1] International Energy Agency. (2023, Apr.) Global EV Outlook 2023. [Online]. Available: https://www.iea.org/reports/global-ev-outlook-2023

[2] V. Cirimele, M. Diana, F. Freschi, and M. Mitolo, "Inductive power transfer for automotive applications: State-of-the-art and future trends," *IEEE Trans. Ind. Appl.*, vol. 54, no. 5, pp. 4069–4079, Sep. 2018.

[3] U. Iruretagoyena, I. Villar, A. Garcia-Bediaga, L. Mir, and H. Camblong, "Design and characterization of a meander-type dynamic inductively coupled power transfer coil," *IEEE Trans. Ind. Appl.*, vol. 53, no. 4, pp. 3950–3959, Jul. 2017.

[4] M. G. S. Pearce, G. A. Covic, and J. T. Boys, "Robust ferrite-less double d topology for roadway IPT applications," *IEEE Trans. Power Electron.*, vol. 34, no. 7, pp. 6062–6075, 2019.

[5] Y. Chen, B. Yang, X. Zhou, Q. Li, Z. He, R. Mai, and J. Lai, "A hybrid inductive power transfer system with misalignment tolerance using quadruple-d quadrature pads," *IEEE Trans. Power Electron.*, vol. 35, no. 6, pp. 6039–6049, 2020.

[6] G. Zhu and R. D. Lorenz, "Achieving low magnetic flux density and low electric field intensity for a loosely coupled inductive wireless power transfer system," *IEEE Trans. Ind. Appl.*, vol. 54, no. 6, pp. 6383–6393, Nov. 2018.

[7] G. Ke, Q. Chen, W. Gao, S. Wong, C. K. Tse, and Z. Zhang, "Research on IPT resonant converters with high misalignment tolerance using multicoil receiver set," *IEEE Trans. Power Electron.*, vol. 35, no. 4, pp. 3697–3712, 2020.

[8] N. Khan, H. Matsumoto, and O. Trescases, "Wireless electric vehicle charger with electromagnetic coil-based position correction using impedance and resonant frequency detection," *IEEE Trans. Power Electron.*, vol. 35, no. 8, pp. 7873–7883, 2020.

[9] S. Lee, M. Kim, B. Lee, and J. Lee, "Impact of rebar and concrete on power dissipation of wireless power transfer systems," *IEEE Trans. Ind. Electron.*, vol. 67, no. 1, pp. 276–287, 2020.

[10] R. Mai, Z. Yan, Y. Chen, S. Liu, and Z. He, "A hybrid transmitter-based efficiency improvement controller with full-bridge dual resonant tank for misalignment condition," *IEEE Trans. Power Electron.*, vol. 35, no. 1, pp. 1124–1135, 2020.

[11] V. X. Thai, G. C. Jang, S. Y. Jeong, J. H. Park, Y. Kim, and C. T. Rim, "Symmetric sensing coil design for the blind-zone free metal object detection of a stationary wireless electric vehicles charger," *IEEE Trans. Power Electron.*, vol. 35, no. 4, pp. 3466–3477, 2020.

[12] V. Zahiri Barsari, D. J. Thrimawithana, and G. A. Covic, "An inductive coupler array for in-motion wireless charging of electric vehicles," *IEEE Trans. Power Electron.*, vol. 36, no. 9, pp. 9854–9863, 2021.

[13] G. Di Capua, N. Femia, K. Stoyka, G. D. Mambro, A. Maffucci, S. Ventre, and F. Villone, "Mutual inductance behavioral modeling for wireless power transfer system coils," *IEEE Trans. Ind. Electron.*, vol. 68, no. 3, pp. 2196–2206, 2021.

[14] B. Song, S. Cui, Y. Li, and C. Zhu, "A fast and general method to calculate mutual inductance for ev dynamic wireless charging system," *IEEE Trans. Power Electron.*, vol. 36, no. 3, pp. 2696–2709, 2021.

[15] *Surface Vehicle Standard*, Society of Automotive Engineers Std. J2954, Rev. oct2020, Apr. 2020.

[16] C. Sullivan, "Optimal choice for number of strands in a litz-wire transformer winding," *IEEE Trans. Power Electron.*, vol. 14, no. 2, pp. 283–291, 1999.

[17] R. Zhang, J. White, J. Kassakian, and C. Sullivan, "Realistic litz wire characterization using fast numerical simulations," in *Proc. of the 2014 Twenty-Ninth Annual IEEE Applied Power Electronics Conference and Exposition (APEC)*, 2014, pp. 738–745.

[18] A. Rosskopf, E. Bar, C. Joffe, and C. Bonse, "Calculation of power losses in litz wire systems by coupling fem and peec method," *IEEE Trans. Power Electron.*, vol. 31, no. 9, pp. 6442–6449, 2016.

[19] S. Hiruma and H. Igarashi, "Fast 3-d analysis of eddy current in litz wire using integral equation," *IEEE Trans. Magn.*, vol. 53, no. 6, pp. 1–4, 2017.

[20] S. Hiruma, Y. Otomo, and H. Igarashi, "Eddy current analysis of litz wire using homogenization-based fem in conjunction with integral equation," *IEEE Trans. Magn.*, vol. 54, no. 3, 2018.

[21] R. P. Wojda and M. K. Kazimierczuk, "Winding resistance and power loss of inductors with litz and solid-round wires," *IEEE Trans. Ind. Appl.*, vol. 54, no. 4, pp. 3548–3557, 2018.

[22] S. Gyimóthy, S. Kaya, D. Obara, M. Shimada, M. Masuda, S. Bilicz, J. Pávó, and G. Varga, "Loss computation method for litz cables with emphasis on bundle-level skin effect," *IEEE Trans. Magn.*, vol. 55, no. 6, pp. 1–4, 2019.

[23] M. Lu and K. D. T. Ngo, "Analytical calculation of proximity-effect resistance for planar coil with litz wire and ferrite plate in inductive power transfer," *IEEE Trans. Ind. Appl.*, vol. 55, no. 3, pp. 2984–2991, 2019.

[24] K. Niyomsatian, J. Gyselinck, and R. V. Sabariego, "Closed-form complex permeability expression for proximity-effect homogenisation of litz wire windings," *IET Science, Measurement & Technology*, vol. 4, no. 3, pp. 287–291, 2020.

[25] J. Lyu, H. Chen, Y. Zhang, Y. Du, and Q. S. Cheng, "Fast simulation of litz wire using multilevel peec method," *IEEE Trans. Power Electron.*, vol. 35, no. 12, pp. 12 612–12 616, 2020.

[26] S. Ehrlich, H. Rossmanith, M. Sauer, C. Joffe, and M. März, "Fast numerical power loss calculation for high-frequency litz wires," *IEEE Trans. Power Electron.*, vol. 36, no. 2, pp. 2018–2032, 2021.

[27] K. Umetani, S. Kawahara, J. Acero, H. Sarnago, O. Lucía, and E. Hiraki, "Analytical formulation of copper loss of litz wire with multiple levels of twisting using measurable parameters," *IEEE Trans. Ind. Appl.*, vol. 57, no. 3, pp. 2407–2420, 2021.

[28] C. Sullivan, "Aluminum windings and other strategies for high-frequency magnetics design in an era of high copper and energy costs," *IEEE Trans. Power Electron.*, vol. 23, no. 4, pp. 2044–2051, 2008.

[29] S. Ayat, R. Wrobel, J. Baker, and D. Drury, "A comparative study between aluminium and copper windings for a modular-wound IPM electric machine," in *In Proc. of the IEEE International Electric Machines and Drives Conference (IEMDC-2017)*, 2017, pp. 1–8.

[30] M. M. Islam, M. N. Islam, and M. A. Taleb, "Replacing copper winding to aluminium winding of refrigerator compressor motor for cost saving and performance analysis using ansys electronics desktop," in *In Proc. of the 4th International Conference on Electrical Information and Communication Technology (EICT-2019)*, 2019, pp. 1–5.

[31] S. Mukundan, H. Dhulipati, L. Chauvin, B. D. S. G. Vidanalage, A. Edrisy, J. Tjong, and N. C. Kar, "Comparative performance analysis of copper and aluminum wound fractional–slot pmsms for high–speed traction application," in *Proc. of the 22nd International Conference on Electrical Machines and Systems (ICEMS-2019)*, 2019, pp. 1–6.

[32] R. C. Bolam, Y. Vagapov, and A. Anuchin, "Performance comparison between copper and aluminium windings in a rim driven fan for a small unmanned aircraft application," in *In Proc. of the XI International Conference on Electrical Power Drive Systems (ICEPDS-2020)*, 2020, pp. 1–6.

[33] J. Acero, I. Lope, C. Carretero, H. Sarnago, and J. M. Burdío, "Comparative evaluation of different cables for magnetic couplers in inductive power transfer systems," in *Proc. of the 2023 IEEE Applied Power Electronics Conference and Exposition (APEC)*, 2023, pp. 3302–3306.

[34] N. Guan, C. Kamidaki, T. Shinmoto, and K. Yashiro, "Ac resistance of copper clad aluminum wires," in *Proc. of the International Symposium on Antennas and Propagation (ISAP-2012)*, 2012, pp. 447–450.

[35] R. Wojda, V. P. Galigekere, J. Pries, and O. Onar, "Copper-clad aluminum windings as an alternative conductor for high-power electric vehicle wireless charging," in *Proc. of the 2020 IEEE Transportation Electrification Conference & Expo (ITEC)*, 2020, pp. 1197–1200.

[36] J. Zgraja, "Dual-frequency induction heating generator with adjustable impedance matching," *IEEE Trans. Ind. Electron.*, vol. 66, no. 11, pp. 8308–8317, 2019.

[37] R. C. M. Gomes, M. A. Vitorino, D. A. Acevedo-Bueno, and M. B. d. R. Corrêa, "Three-phase ac–ac converter with diode rectifier for induction heating application with improved input current quality and coil modeling," *IEEE Trans. Ind. Appl.*, vol. 57, no. 3, pp. 2673–2681, 2021.

[38] J. Acero, J. Serrano, C. Carretero, I. Lope, and J. M. Burdío, "Analysis and design of tubular coils for wireless inductive power transfer systems," in *In Proc. of the IEEE Applied Power Electronics Conference and Exposition (APEC-2017)*, 2017, pp. 848–854.

[39] M. Etemadrezaei and S. M. Lukic, "Multilayer tubular conductor for high Q-factor wireless power transfer system resonators," *IEEE Trans. Ind. Appl.*, vol. 52, no. 5, pp. 4170–4178, Sep. 2016.

[40] G. Zhu and R. D. Lorenz, "Surface spiral parallel and antiparallel winding designs for high efficiency, low spatial voltage stress, and inductive wireless power transfer systems," *IEEE Trans. Ind. Appl.*, vol. 55, no. 1, pp. 741–750, Jan. 2019.

[41] B. A. Reese, R. Joseph, and C. R. Sullivan, "Improved Litz-Wire Designs for the MHz Range," 2018, pp. 1–8.

[42] C. Carretero, J. Acero, and R. Alonso, "Tm-te decomposition of power losses in multi-stranded litz-wires used in electronic devices," *Progress In Electromagnetics Research, PIER*, vol. 123, no. 1, pp. 83–103, 2012.

[43] I. Lope, J. Acero, and C. Carretero, "Analysis and optimization of the efficiencyof induction heating applications with litz-wire planar and solenoidal coils," *IEEE Trans. Power Electron.*, vol. 7, no. 31, pp. 5089–5101, Jul. 2016.

[44] H. Dwight, "Reactance and skin effect of concentric tubular conductors," *Electrical Engineering*, vol. 61, no. 7, pp. 513–518, 1942.

[45] B. Teare and J. Webb, "Skin effect in bimetallic conductors," *Electrical Engineering*, vol. 62, no. 6, pp. 297–302, 1943.

[46] J. Acero, C. Carretero, I. Lope, R. Alonso, and J. Burdío, "Analytical solution of the induced currents in multilayer cylindrical conductors under external electromagnetic sources," *Applied Mathematical Modelling*, 2016. [Online]. Available: http://www.sciencedirect.com/science/article/pii/S0307904X16304127

[47] Elektrisola. [Online]. Available: https://www.elektrisola.com/en/Metal

[48] G. Vandevoorde and R. Puers, "Wireless energy tranfer for stand-alone systems: A comparison between low and high power applicability," *Sensors and Actuators A: Physical*, vol. 92, pp. 305–311, Jul. 2001.